Dalton Transactions

ROYAL SOCIETY OF CHEMISTRY

PAPER

View Article Online
View Journal | View Issue

Cite this: *Dalton Trans.*, 2025, **54**, 1815

A terpyridine-based copper complex for electrochemical reduction of nitrite to nitric oxide†

Jyotiprokash Biswas,[a] Sebastian Sanden,[a] Prabhakar Bhardwaj,[b] Daniel Siegmund,[a,c] Pankaj Kumar*[b] and Ulf-Peter Apfel *[a,c]

Received 1st October 2024,
Accepted 4th December 2024

DOI: 10.1039/d4dt02777a

rsc.li/dalton

In biological systems, nitrite reductase enzymes (NIRs) are responsible for reduction of nitrite (NO_2^-) to nitric oxide (NO). These NIRs have mostly Cu- or Fe-containing active sites, surrounded by amine-containing ligands. Therefore, mononuclear Cu complexes with N-donor ligands are highly relevant in the development of NIR model systems and in the mechanistic investigation of the nitrite reduction reaction. Herein, we report on a terpyridine-based Cu^{II} complex with square planar geometry for H^+-assisted electrochemical reduction of NO_2^-. Through electrochemical measurements, spectroscopic characterization and isotope-labelling experiments we propose a mechanistic reaction pathway involving an unstable HNO_2 state. The Cu^I intermediate, formed electrochemically, was isolated and its molecular structure was deduced, showing linkage isomerism of the nitrite ligand. Moreover, qualitative and quantitative product analysis by GC-MS shows N_2O formed as a side product along with the main product NO. Furthermore, by obtaining single crystals and conducting structural analysis we were able to determine the structural arrangement and redox state of the complex after electrochemical treatment.

Introduction

Nitrogen metabolism and fixation occurs simultaneously in almost every form of life.[1,2] This two-way process of supply and fixation spans from local to global ecological systems. Mostly due to human activity and exploitation, the environmental nitrogen cycle has been disturbed causing a nitrogen imbalance and eventually an increase in nitrogen content in several areas of the environment.[3–5] The denitrification steps in the global nitrogen cycle have the pivotal function of releasing the aggregated nitrogen species back into the atmosphere. Among the denitrification steps performed by microorganisms, the transformation of nitrite (NO_2^-) to nitric oxide (NO) is very important and has been studied extensively for decades.[6] Moreover, the reduced product of NO works as an important cell-signalling agent and vasodilator.[7–11] Therefore, NO_2^- acts as a source of NO in the bloodstream under hypoxic conditions.[12–14] It has been established that nitric oxide synthases (NOSs) are responsible for NO evolution in muscles and tissues by converting arginine to citrulline along with the generation of NO.[15,16] Additionally, certain non-NOS groups of enzymes are also capable of performing the reduction of NO_2^- to NO, such as cytochrome *c* oxidase (CcO), xanthine oxidase (XO) and nitrite reductases (NIRs). Cytochrome *c* oxidase, present in the mitochondrial network, is a heterobimetallic (*heme*-Fe/Cu) system.[17–19] On the other hand, mammalian xanthine oxidase (Mo)[20–22] and microbial NIRs (Fe or Cu) have monometallic active sites.[23–25]

In the denitrification process, the one-electron reduction step of NO_2^- to NO is mediated by NIRs and depending on the metal atom present at the active site they are called either CuNIRs (Cu-containing active site) or FeNIRs (Fe-containing active site). In CuNIRs, the main stage for the whole catalytic process, *i.e.* the active site, is a type II Cu atom, which is coordinated with three histidinyl nitrogens and a water molecule as reported in X-ray structure studies.[26–30] NO_2^- coordinates with the Cu^{II} centre by substituting the water molecule followed by subsequent electron and proton transfer steps (Scheme 1).[31,32]

Several Cu- and Fe-based mononuclear complexes with amine-containing ligands have been reported as models of CuNIRs and FeNIRs, respectively, when exploring mechanisms

[a]*Inorganic Chemistry I, Ruhr-Universität Bochum, Universitätsstraße 150, 44801 Bochum, Germany. E-mail: ulf.apfel@ruhr-uni-bochum.de*
[b]*Department of Chemistry, Indian Institute of Science Education and Research (IISER), Tirupati 517507, India*
[c]*Department of Electrosynthesis, Fraunhofer UMSICHT, Osterfelder Str. 3, 46047 Oberhausen, Germany*

†Electronic supplementary information (ESI) available. CCDC 2376874–2376878 and 2376880. For ESI and crystallographic data in CIF or other electronic format see DOI: https://doi.org/10.1039/d4dt02777a

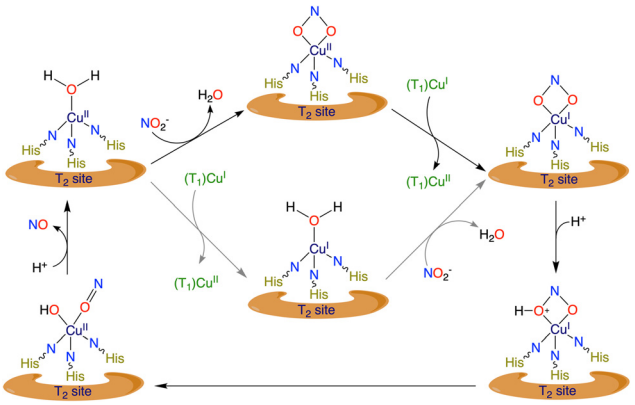

Scheme 1 Simplified mechanistic illustration of reduction of NO_2^- to NO by CuNIRs.[6,43]

and energetics of the nitrite reduction process. Tolman first reported a copper–nitrosyl complex in 1992,[33] and subsequent studies, including work by Murphy,[28,34] Fujisawa[35] and Nam's group,[36]revealed intermediates such as {CuNO}^{10} and {FeNO}^{6} during nitrite reduction. Recently, we reported proton-assisted NO_2^- reduction, mediated by a heterobimetallic CuCo complex, highlighting the benefit of the bimetallic complex over a monometallic one.[37]

Furthermore, there has been significant development in the research of CuNIR model complexes that can perform nitrite reduction electrochemically. Since 1993, after Komeda *et al.* reported on electrochemical nitrite reduction for the first time,[38,39] several electrochemical studies for nitrite reduction have been published. Meyerhoff and coworkers investigated electrochemical reduction of nitrite in aqueous solution using a series of mononuclear Cu^{II} complexes (Scheme 2a to d), aiming to develop demand-based biomedical devices for controlled NO release.[40–42] Recently, the groups of Smith and Bren have reported buffer-assisted electrocatalytic nitrite reduction featuring Co^{III}-based (Scheme 2g)[44] and Fe^{III}-based (Scheme 2f)[45] complexes, respectively. The buffer appeared to be highly crucial for the catalyst's stability. Moreover, some reports have demonstrated electrochemical nitrite reduction in organic solution as well. Symes and coworkers reported nitrite

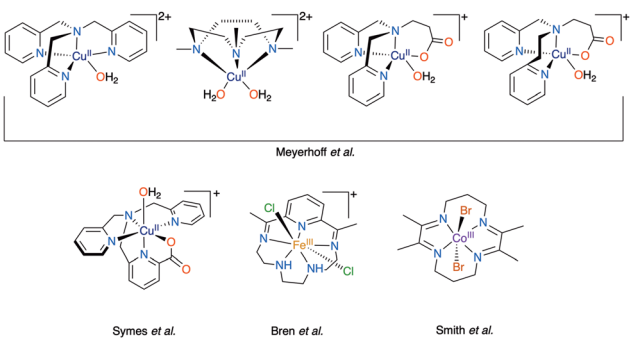

Scheme 2 Cu-, Co -and Fe-based molecular catalysts, reported for electrochemical nitrite reduction.[40–45]

reduction in acetonitrile using a mononuclear Cu^{II} complex with a pendant carboxyl group (Scheme 2e), which enhances the proton relay mechanism and significantly improves activity toward nitrite activation.[43] The electrochemical reactivity of CuNIR model complexes have shown crucial pH dependence, which is expected from the elemental reaction equation (eqn (1)):

$$NO_2^- + 2H^+ + e^- \rightarrow NO + H_2O \quad (1)$$

Reduction of NO_2^- is believed to go through an {M–NO}^{n} intermediate, which is generated from the decomposition of a very transient {M–ONOH} species.[37,43,46] As a result, over the years, different research groups have tried to isolate metal-nitrosyl species and investigate their properties, stability and reactivity.[47–51] There are few reports that dig deeply into the rate-determining steps[46] or proton–electron transfer mechanisms.[43] However, to the best of our knowledge, not much focus has been given to the post-electrolytic conditions of the catalyst or the model complex either. The very few reports that are available on this matter are mostly theoretical.[43,46]

Taking all the above-mentioned data and discussion into consideration, herein, we report on the synthesis and characterization of a Cu^{II} complex, **[TerpyCu(CH$_3$CN)](ClO$_4$)$_2$**, (**1**) (Terpy = 2,2′:6′,2″-terpyridine) (Scheme 3) and its activity towards electrochemical nitrite reduction. We conducted electrochemical nitrite reduction using CH_3COOH as a proton source, identifying products *via* GC-MS and ^{1}H-NMR. Notably, we also obtained the structural proof of linkage isomerism of the nitrite ligand during redox transitions.

Results and discussion

Synthesis and characterizations of the Cu complexes

Complex **1** was prepared by a single-step reaction between Terpy and $Cu(ClO_4)_2{\cdot}6H_2O$ in acetonitrile at room temperature (Scheme 3, Step I). In the UV-Vis spectrum, upon addition of the Cu^{II} salt to the ligand solution a new band appears at 626 nm, which corresponds to the d–d transition (Fig. 1A). ESI-MS showed distinct *m*/*z* peaks at 296.0 and 395.0 corresponding to $[TerpyCu]^+$ and $[TerpyCu(ClO_4)]^+$ (Fig. S8†). Additionally, the magnetic moment of **1** was calculated by Evans' method using ^{1}H-NMR spectroscopy (Fig. S14†). The magnetic moment of **1** was found to be 1.69 BM, which falls in line with the +II oxidation state of the Cu centre. We obtained single crystals for complex **1** and deduced its molecular structure *via* single-crystal X-ray diffraction (SXRD), which shows coordination of Cu^{II} with the ligand and an additional CH_3CN molecule (Scheme 3). Notably, the molecular structure shows that the oxygen atoms of the perchlorate moiety are oriented toward the metal centre. The distances between the perchlorate oxygen atoms and the Cu^{II} centre range from 2.5 to 2.7 Å, suggesting the presence of weak interactions between the perchlorate oxygen and the metal centre. Additionally, the IR stretching frequency of the perchlorate anion (1113 cm^{-1}, Fig. S1†) in complex **1** aligns with the stretching frequency of

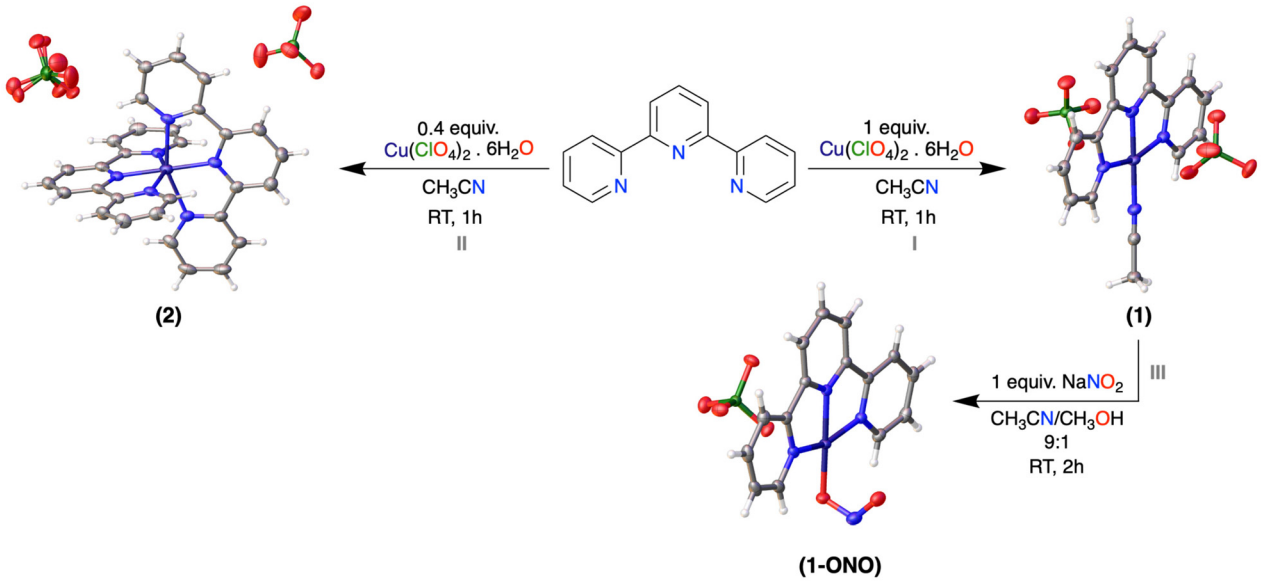

Scheme 3 Synthetic scheme of **[TerpyCu(CH$_3$CN)](ClO$_4$)$_2$**, (**1**), **[(Terpy)$_2$Cu](ClO$_4$)$_2$**, (**2**) and **[TerpyCu(ONO)]ClO$_4$**, (**1-ONO**), showing their corresponding molecular structures, deduced from SXRD analysis. Solvent molecules are omitted for clarity. Colour code: C grey, H white, N blue, O red, Cu violet, Cl green.

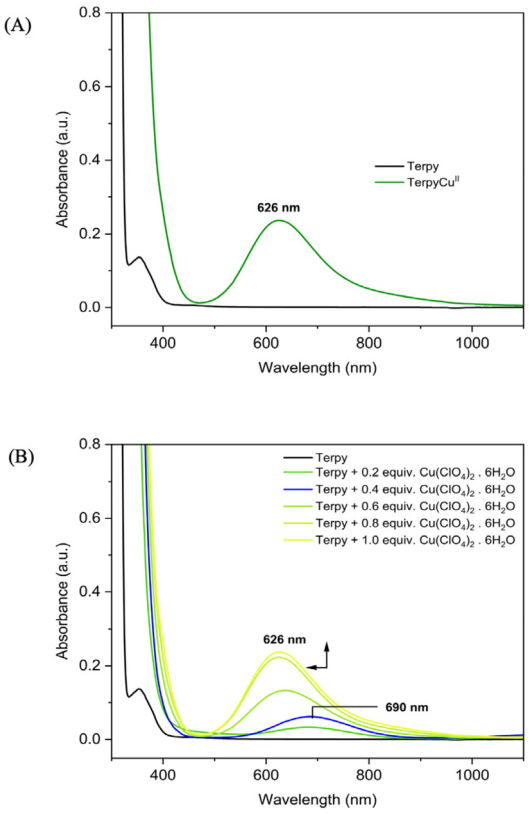

Fig. 1 (A) UV-Vis spectrum of **1**, showing a d–d transition band upon addition of Cu^{II} salt. (B) Change in UV-Vis spectra upon stepwise addition of Cu^{II} salt to the ligand solution (concentration: 2 mM; solvent: acetonitrile).

perchlorates in a terpyridine-*N*-oxide copper complex previously reported by Murphy and coworkers,[52] who also highlighted weak interactions between perchlorate and Cu centres and included the ClO_4^- in describing the overall geometry of the complexes. Taking all the data and information into consideration, it can be inferred that there are weak interactions between the metal centre and the perchlorate ions and that the structure around the Cu^{II} centre in complex **1** could also be described as a tetragonally distorted octahedron with two very long-distance Cu–O interactions (involving oxygen atoms of the perchlorates). However, due to the large distance between the Cu^{II} centre and the perchlorate oxygen atoms, the interaction can be considered transient in solution with the complex being a cationic species.

To closely monitor the coordination of Cu^{II} with the terpyridine ligand, a stepwise addition of a Cu^{II} salt to the ligand solution was carried out, with the progress of the reaction being tracked using UV-Vis spectroscopy. Initially, the addition of the Cu^{II} salt up to 0.4 equiv., resulted in the appearance of a distinct absorption band at 690 nm in the UV-Vis spectrum (Fig. 1B, blue line). However, as more Cu^{II} salt was added beyond 0.4 equiv., a blue shift of the band at 690 nm to 626 nm was observed (Fig. 1B). Based on this result, we assumed that there could be a different Cu-containing species at the initial stage of the measurement. To gain more insight, a complexation reaction was set up with 1 equiv. of ligand and 0.4 equiv. of Cu^{II} salt (Scheme 3, Step II), and the product was isolated and characterized by UV-Vis, ESI-MS, FT-IR and SXRD. The UV-Vis spectrum of the prepared complex (Fig. S18A†) shows an identical band pattern to the spectrum (blue line in Fig. 1B) observed upon addition of 0.4 equiv. of Cu^{II} salt in the ligand solution during the UV-Vis

titration. After completion of the reaction, we observed a clear *m*/*z* peak at 264.6 in the ESI-MS analysis (Fig. S9†), corresponding to a previously reported bis-terpyridine copper complex,[53,54] $[(Terpy)_2Cu]^{2+}$ (**2**), which was further confirmed by the molecular structure derived from SXRD (Scheme 3). One of the perchlorate ions is modelled as being disordered in the molecular structure. In contrast to complex **1**, all the coordination sites are occupied by the ligands in complex **2**, hence, the perchlorate counterion is hindered from coordinating with the metal centre. Therefore, the d–d transition band at 690 nm appears in the early stage of the measurement due to the formation of **2** in the solution. As we continue to add more Cu^{II} salt, the ligand-to-metal 1 : 1 reaction is favoured, eventually giving a band at 626 nm, which is similar to that observed for complex **1**.

When $NaNO_2$ was added to the solution of **1**, the blue-coloured solution turned green, indicating the coordination of nitrite with the Cu^{II} centre, resulting in $[TerpyCuONO]^+$ (**1-ONO**) (Scheme 3, Step III). The UV-Vis spectrum revealed the appearance of a new LMCT band at 372 nm corresponding to the nitrite coordination. Additionally, a red shift of the d–d transition band from 626 nm to 640 nm was observed (Fig. 2). FT-IR spectroscopy of **1-ONO** showed signals at 1268 cm^{-1} (ν_{sym}, NO_2) and 1366 cm^{-1} (ν_{asym}, NO_2), which shifted to 1251 cm^{-1} (ν_{sym}, $^{15}NO_2$) and 1352 cm^{-1} (ν_{asym}, $^{15}NO_2$), respectively, when ^{15}N-labelled $Na^{15}NO_2$ was used, resulting in **1-O^{15}NO** (Fig. 2, Inset III and Fig. S3, S4†). In the ESI-MS analysis, an *m*/*z* peak at 342.1 for $[TerpyCuONO]^+$ was observed and this peak was shifted to *m*/*z* 343.1 in the case of the ^{15}N-labelled compound (Fig. S10 and S11†). The molecular structure of **1-ONO** derived from SXRD analysis (Scheme 3) shows a four-coordinated Cu^{II} centre where the acetonitrile molecule is substituted by nitrite, which binds through one of the oxygens (–ONO, nitrito binding mode). Similar to complex **1**, the perchlorate ion in **1-ONO** also exhibits weak interaction with the metal centre, as indicated by the long Cu–O distance (2.4 Å) and IR stretching frequency (ν_s-ClO_4^-, 1111 cm^{-1}; Fig. S3†). Due to this very weak interaction between the perchlorate ion and Cu^{II}, **1-ONO** can be considered a cationic compound as well. We have also calculated the binding constant (K_b) for nitrite coordination by using the Benesi–Hildebrand equation.[55,56] The slope ($1/K_b$) of the Benesi–Hildebrand plot (Fig. 2, Inset II) was found to be 0.4528 mM. Therefore, K_b for complex **1** is 2.21×10^3 M^{-1}.

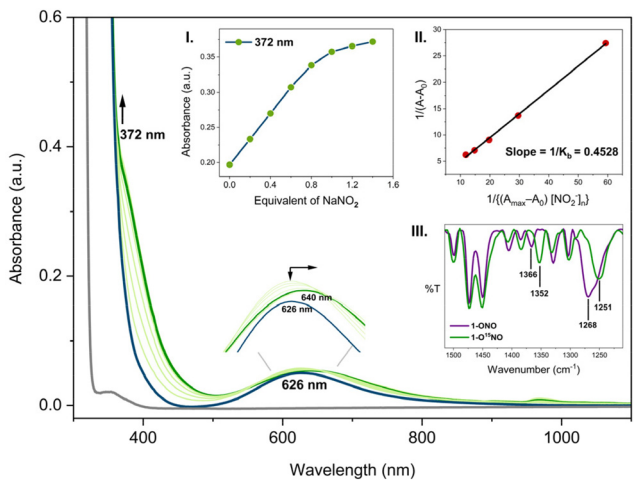

Fig. 2 UV-Vis spectral change upon addition of $NaNO_2$. Grey line, 0.5 mM Terpy; teal blue line, 0.5 mM **1**. Stepwise addition of $NaNO_2$ is shown by the light green lines. Dark green line, spectrum after addition of 1 equiv. $NaNO_2$. Inset I: rise of the band at 372 nm corresponding to NO_2^- coordination. Inset II: Benesi–Hildebrand plot for the binding constant calculation. Slope = $1/K_b$ = 0.4528 mM. Inset III: FT-IR spectra of **1-ONO** (violet line) and **1-O^{15}NO** (green line) in KBr.

Electrochemical NO_2^- reduction

Cyclic voltammetric analysis. The activity of complex **1** towards NO_2^- reduction was investigated electrochemically using a three-electrode system. All the potentials are given with reference to the Fc^+/Fc couple. Cyclic voltammetry (CV) experiments for **1** were performed in acetonitrile, containing 100 mM tetrabutylammonium hexafluorophosphate ($TBAPF_6$). We recorded cyclic voltammograms of **1** over different ranges of potentials in order to identify different redox couples present in the electrolytic solution (Fig. 4A). First, a CV scan was performed from −0.58 V to −1.57 V, which showed two successive reductive signals at −0.88 V and −1.13 V, while a sharp oxidative signal was observed at −0.82 V. The high intensity of the oxidative signal suggests that it is a stripping signal, indicative of some preceding decomposition process. When the reductive scan was stopped and reversed at −1.07 V, *i.e.* after the first reductive signal, the sharp oxidative signal at −0.82 V disappeared, and a reversible redox wave (E_{pc} = −0.88 V, E_{pa} = −0.80 V, $E_{1/2}$ = −0.84 V *vs.* Fc^+/Fc^0) was observed, which can be attributed to the Cu^{II}/Cu^{I} redox couple as the values fall in line with the previously reported values for the Cu^{II} tripodal complex.[43] Therefore, the second reductive signal at −1.13 V can be assigned to the Cu^{I}/Cu^{0} couple. On the other hand, due to the proximity of the oxidative peaks of Cu^0/Cu^I and Cu^I/Cu^{II}, we did not observe two separate oxidative signals, rather one single peak at −0.82 V, which can be attributed to Cu^0 to Cu^{II} oxidation.

Additionally, when NO_2^- was added to the complex solution we observed a shift of 200 mV for the Cu^{II}/Cu^{I} couple towards less cathodic potentials (Fig. 4C). In the presence of NO_2^- the $E_{1/2}$ for Cu^{II}/Cu^{I} is −0.62 V (*vs.* Fc^+/Fc). Upon the addition of nitrite, the solution turned green. Cyclic voltammograms were then recorded for varying equivalents of NO_2^- in the presence of CH_3COOH as the proton source. A new reductive catalytic signal was observed at −1.27 V, which corresponds to NO_2^- reduction. As we increased the amount of nitrite in the solution, higher current values were observed at −1.27 V (Fig. 4D).

Bulk electrolysis. To analyze the products formed in the electrochemical reaction, bulk electrolysis was performed in an electrochemical cell, sealed under an argon atmosphere. Chronoamperometric experiments were performed at a fixed potential of −1.29 V with 2 mM complex **1**, 40 mM $NaNO_2$, 150 mM CH_3COOH and 0.2 M $TBAPF_6$ in acetonitrile with a

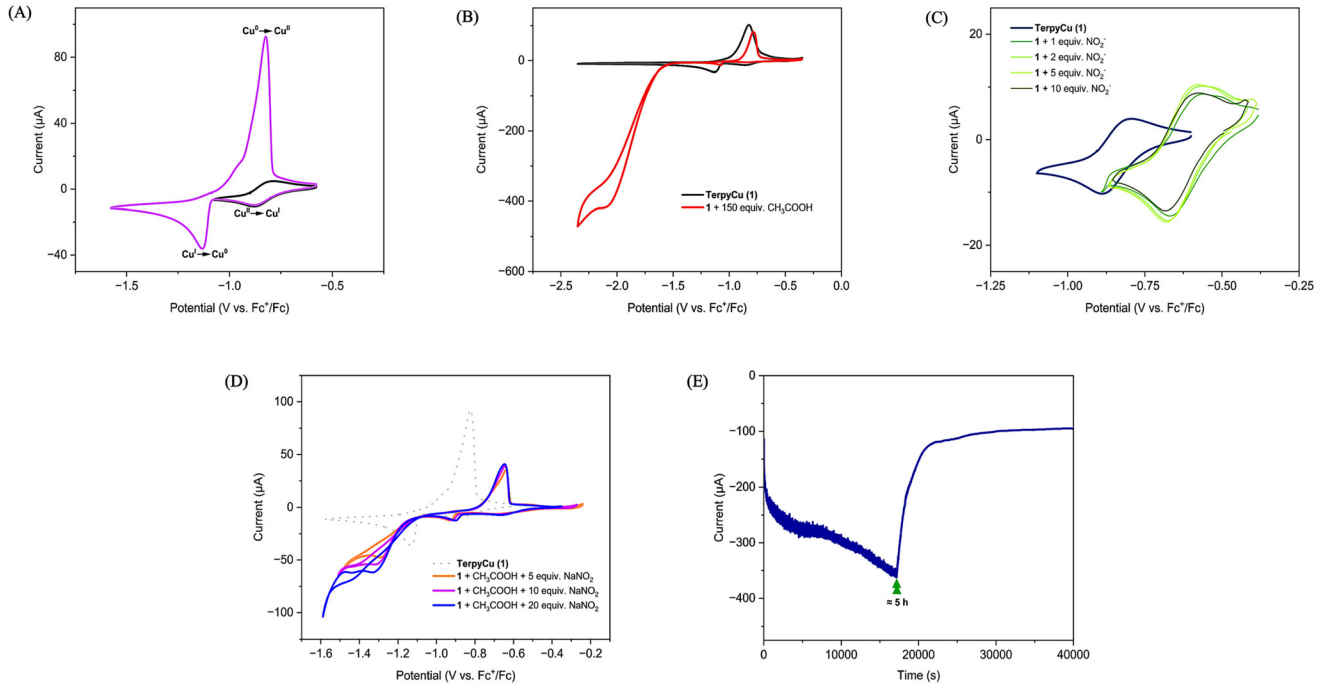

Fig. 4 (A) Cyclic voltammograms of **1** (1 mM). Voltammograms over different potential ranges are shown in different colours. Purple line: potential range −0.58 V to −1.57 V. Black line: potential range −0.58 V to −1.07 V. (B) Cyclic voltammograms of 1 mM complex **1** (black line) and 1 mM complex **1** in the presence of 150 equiv. CH_3COOH (red line). (C) Reversible redox wave of the Cu^{II}/Cu^{I} ($E_{1/2}$ = −0.84 V) couple under cyclic voltammetry (teal blue line). The green traces show the shift of Cu^{II}/Cu^{I} ($E_{1/2}$ ∼ −0.62 V) to the anodic side upon addition of NO_2^-. (D) Cyclic voltammograms in the presence of 1 mM complex **1**, and 150 equiv. CH_3COOH and NO_2^-, showing generation of a reductive catalytic signal at −1.27 V. Cyclic voltammograms upon addition of 5 equiv., 10 equiv. and 20 equiv. are shown by orange, violet and blue lines, respectively. Cyclic voltammogram of complex **1** is shown with a grey dotted line for reference. (E) Chronoamperometric (CA) plot for 2 mM **1**, 150 mM CH_3COOH, and 40 mM NO_2^- at −1.29 V, showing a drop in cathodic current after 5 h. Solvent: CH_3CN; supporting electrolyte: $TBAPF_6$ (0.1 M for CV and 0.2 M for CA). Electrodes: glassy carbon as working electrode, Pt wire as counter electrode, Ag wire as pseudo-reference electrode. All the potential values are presented with reference to the Fc^+/Fc couple.

small amount of water to dissolve the $NaNO_2$ (acetonitrile/water 100 : 1). In the chronoamperometric plot, we observed a current drop after the 5 h mark (Fig. 4E). We suspected the current drop could be due to some deposition on the electrode surface. After completion of the experiment, we indeed noticed some deposits on the electrode surface. The deposited material was analyzed by an SEM/EDX technique, and it was found that the material mainly consisted of metallic copper (Fig. S22†). This deposition is the reason for the anodic stripping signal observed at −0.82 V. Additionally, it was observed that the electrolyte solution, initially colourless during electrolysis, gradually turned blue over time when left standing or upon exposure to air, indicating the presence of copper species in the solution. Fortunately, we were able to obtain single crystals from this blue-coloured solution which, after SXRD analysis, turned out to be a Terpy-Cu^{II} complex with an acetate moiety and a water molecule coordinated with the Cu^{II} centre, namely $\mathbf{[TerpyCu^{II}(H_2O)(OCOCH_3)]PF_6}$ (**3**) (Fig. 3). In the molecular structure there is minor disorder in the PF_6 counterion, which was left unmodelled due to apparently low component occupancy and clear identity of the counterion. [For other spectroscopic characterization data of complex **3**, please refer to the ESI (Fig. S5, S12 and S19†).]

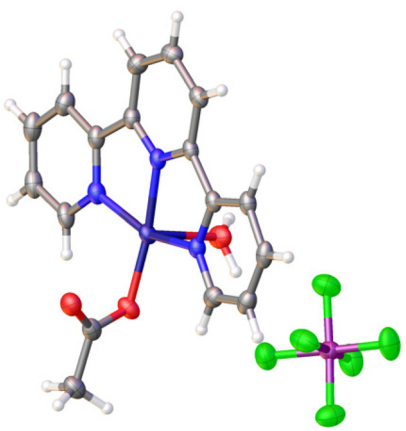

Fig. 3 Molecular structure of $\mathbf{[TerpyCu^{II}(H_2O)(OCOCH_3)]PF_6}$, (**3**) deduced from SXRD analysis. Colour code: C grey, H white, N blue, O red, Cu violet, P purple, F light green.

Therefore, it can be concluded that after the electrolysis some of the catalyst was deposited on the electrode surface, while some remained in solution as complex **3**.

Linear sweep voltammetry (rinse test). To identify the catalytically active species, a rinse test was conducted. Initially, a chronoamperometric experiment was performed at the potential corresponding to $Cu^{I} \rightarrow Cu^{0}$, leading to the deposition of metallic copper on the electrode surface. Following this, the electrochemical cell was replenished with fresh solution containing 5 mM $NaNO_2$ and 150 mM CH_3COOH, while keeping the working electrode unchanged. Linear sweep voltammetry (LSV) experiments were then carried out.

Initially, when the LSV scan was initiated from −1.1 V, a voltammogram (purple trace, Fig. 5) that did not match the catalytic LSV profile of complex **1** (blue trace, Fig. 5) was obtained. This result indicates that the deposited Cu^0 is not the catalytically active species.

Further experiments were performed by initiating the LSV scan from a less negative (more oxidative) potential of −0.65 V. In this case, the resulting voltammogram (brown trace, Fig. 5) displayed a current response similar to that observed for complex **1** in solution. These findings suggest that at more oxidative potentials, the deposited Cu^0 is re-oxidized to Cu^{II}, which subsequently undergoes reduction to form Cu^{I}. The Cu^{I} species generated in this process facilitates the catalytic reaction, confirming it as the catalytically active species.

Product analysis and quantification

NO detection by UV-Vis spectroscopy. As mentioned above, the expected reduction product from the electrolysis of NO_2^- is nitric oxide (NO). To detect if any NO gas is produced during the bulk electrolysis, a well-known NO capturing molecule, cobalt(II) tetraphenylporphyrin (CoTPP), was used. Upon binding NO, the band for CoTPP at around 528 nm in the UV-Vis spectra undergoes a clear bathochromic shift, which is characteristic for NO coordination. Here, in this case, a CoTPP solution was treated with the gas mixture accumulated in the headspace of the electrolytic cell and then UV-Vis spectra were recorded. In the UV-Vis spectra, we observed a clear shift of the band at 527 nm to 535 nm (Fig. S18D†), proving NO production during the electrocatalytic reduction of NO_2^-.

GC-MS analysis. Furthermore, we used GC-MS as a second validation method of NO production and eventually to quantify NO. When the accumulated gas mixture was injected into the GC-MS system, a peak of *m*/*z* 30 corresponding to NO at 3.80 min (R_t, retention time) was observed. Additionally, we performed bulk electrolysis using $Na^{15}NO_2$ keeping all other conditions constant and injected the headspace gas mixture into the GC-MS system.

In the chromatogram, at 3.80 min (R_t), a peak of *m*/*z* 31 was observed, which can be attributed to ^{15}NO (Fig. S23†). These results provide conclusive evidence of NO formation in the electrochemical NO_2^- reduction process. Moreover, two successive peaks of *m*/*z* 44 were observed in the chromatogram at 5.05 min and 5.37 min (R_t) in the case of the analysis of the gas mixture obtained from bulk electrolysis using $NaNO_2$. Interestingly, the *m*/*z* 44 peak at 5.05 min (R_t) remained the same but the peak at 5.37 min (R_t) changed to *m*/*z* 46 when ^{15}N-labelled $Na^{15}NO_2$ was used in the electrocatalytic process (Fig. S24†). This suggests that the *m*/*z* 44 peak at R_t 5.37 min is for nitrous oxide (N_2O) and, correspondingly, the *m*/*z* 46 peak is for $^{15}N_2O$. It is postulated that N_2O originates from disproportionation of NO.[57–60] The *m*/*z* 44 peak at 5.05 min corresponds to CO_2 originating from atmospheric interference (Fig. S24†).

NO and N_2O were then quantified *via* GC-MS (Fig. 6), obtained from electrolysis experiments of different durations. Separate bulk electrolysis experiments with 2 mM complex **1**, 40 mM $NaNO_2$, 150 mM CH_3COOH and 0.2 M $TBAPF_6$ at a fixed potential of −1.29 V were performed for 1 h, 3 h, 5 h and 7 h in the same cell and the headspace gas mixture was ana-

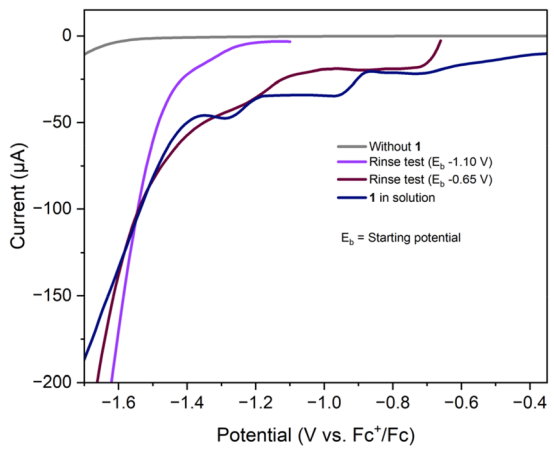

Fig. 5 Linear sweep voltammograms (LSV) of 5 mM $NaNO_2$ in solution (grey trace); rinse test LSV with starting potential (E_b) −1.10 V (purple trace) and E_b −0.65 V (brown trace) in the presence of 5 mM $NaNO_2$; LSV of 2 mM **1** and 5 mM $NaNO_2$ in solution. Solvent: MeCN/H_2O (100 : 1); proton source: CH_3COOH (150 mM); supporting electrolyte: 0.1 M $^nBu_4PF_6$; electrodes: glassy carbon (WE), Pt wire (CE), Ag wire (RE). Potentials are given with reference to Fc^+/Fc.

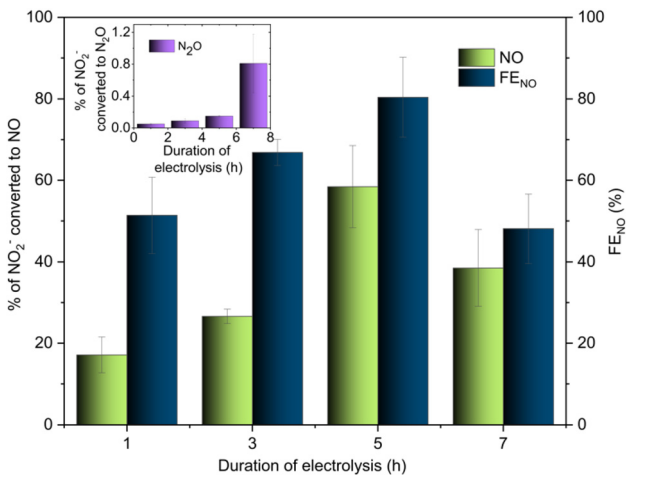

Fig. 6 GC-MS analysis of NO (left-hand *y*-axis, green columns) and N_2O (inset, purple columns) produced from NO_2^- after running the electrolysis experiment for different time durations. Faradaic efficiency (FE) of the total NO in each case is shown along the right-hand *y*-axis (blue columns).

lyzed. We achieved a maximum FE of 81% for NO production (Fig. 6). Up to 5 h, an increasing trend in the concentration of NO and N_2O accumulating in the headspace was observed. After 5 h a decrease in headspace NO concentration was observed, which is in accordance with the current drop in bulk electrolysis after 5 h. Interestingly, even though NO production abated, we still observed an increase in N_2O concentration after 7 h. This result implies that after 5 h, NO production subsides due to the deposit formation on the electrode surface, but disproportionation of the formed NO continues.

Subsequent reduction of NO to NH_3 in homogeneous electrocatalysis is rarely reported in the literature,[61] as it necessitates the transfer of 5 H^+. Using secondary amines as proton donors, Co-based macrocycles were able to perform the final reduction step to NH_3 in aqueous solution.[62] Alternatively, N–O cleavage was also achieved using a bimetallic Ru complex, which was able to stabilize an unusual μ-nitrido species between two Ru atoms.[63]

Mechanistic insight of NO_2^- reduction

In Scheme 4, a proposed mechanistic cycle is shown. First, nitrite coordinates with **1** through one of its oxygens (O-bound, nitrito binding mode), as evident from the molecular structure **1-ONO**. Upon reduction of the Cu^{II} to Cu^{I} centre, the –ONO ligand undergoes linkage isomerism and binds through nitrogen (N-bound, nitro binding mode). Fortunately, we have been able to isolate and crystallize this Cu^{I} compound from the electrolytic solution. One could assume that this rearrangement might be initiated by the protonation of nitrite. To gain more information, terpyridine was reacted with a Cu^{I} salt and $NaNO_2$. In both cases, *i.e.* from the electrolytic solution and from the reaction mixture with the Cu^{I} salt, the same product, a nitrite-bound di-copper complex, **[TerpyCu(NO$_2$)]$_2$** (**4**), was obtained, which was characterized *via* SXRD analysis (Fig. 7A). From this result it can be conclusively stated that the rearrangement of the nitrite ligand is independent of the protons in the electrolytic solution. Maji *et al.* proposed a similar rearrangement of the nitrite ligand[64] and, herein, our crystallographic studies support that claim with clear structural data. Fig. 7A shows the structure of the isolated Cu^{I} state, thereby confirming the linkage isomerism of the nitrite ligand. Generally, Cu^{I} preferentially adopts tetrahedral over planar geometry. As a result, when the Cu^{II} centre (having a square planar geometry) in **1** was reduced to Cu^{I}, the metal centre protrudes out of the square plane in order to attain tetrahedral geometry and ends up coordinating with two N atoms of one terpyridine molecule and with another terpyridine-N atom of another Terpy–Cu^{I} fragment, resulting in a homobimetallic Cu^{I} complex (Cu–Cu distance ~3.0 Å) with nitrite bonded through its N-atom with the metal centre (Fig. 7A). Having d^{10} electronic configuration at Cu^{I} centres, complex **4** is diamagnetic in nature, which was further confirmed when a long-range ^{1}H-NMR spectrum was recorded for **4** and no paramagnetically shifted peak was found (Fig S15†). Additionally, no shift of the reference peak was observed in the ^{1}H-NMR spectrum, recorded by following Evans' method (Fig. S16†). Stability of **4** was also monitored by UV-Vis spectroscopy. Under an inert atmosphere, a band at 370 nm was observed in the UV-Vis spectrum for a freshly prepared solution of **4** in acetonitrile (Fig. S18B†). Then the solution was allowed to come into contact with air by opening the cuvette and the change of the solution in the presence of air was monitored for 6 h *via* UV-Vis spectroscopy. In the UV-Vis spectra, we observed initial increase followed by gradual decrease in band intensity at 370 nm and the rise of a new d–d transition band at 670 nm, which indicates oxidation of the Cu^{I} centre of **4** (Fig. S18C†).

Moreover, we observed very few green cuboid-shaped crystals in the crystallization vial of the complex **4** and, upon analyzing those green crystals by SXRD, they were found to be a Cu^{II}-dinitrito complex, **[TerpyCu(ONO)$_2$]** (Fig. 7B). Although for the nitrite ligands the 'nitrito' mode (*i.e.* –ONO) was found to be predominant in the molecular structure, the isomeric linkage mode, *i.e.* 'nitro' mode (–NO_2), was found to have an occupancy of ~7% in the structure. The linkage isomerism was modelled accordingly in the structure (see the ESI, Fig. S29†). This Cu^{II} complex is a disproportionation product of complex **4**.

NO_2^- reduction is believed to proceed *via* an unstable HNO_2 intermediate with an abundance of protons. Cioncoloni *et al.* observed that the electron transfer and the protonation of nitrite happen simultaneously.[43] This HNO_2 intermediate further dissociates to form NO and H_2O. We have already detected the formation of NO so, to prove the generation of

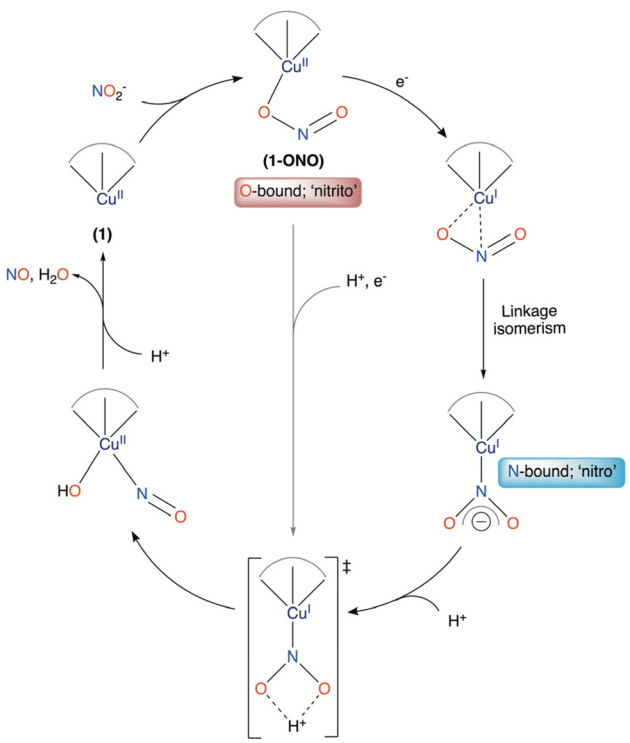

Scheme 4 Proposed mechanistic route for the electro-reduction of NO_2^- to NO by **TerpyCu** (**1**).

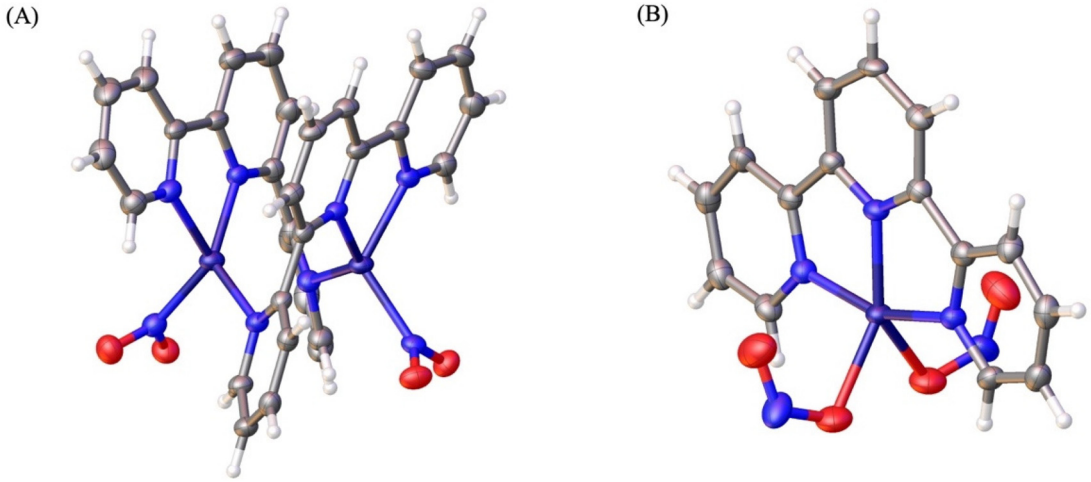

Fig. 7 Molecular structure of (A) **[TerpyCu(NO$_2$)]$_2$**, (**4**) and (B) **[TerpyCu(ONO)$_2$]** deduced from SXRD analysis. Colour code: C grey, H white, N blue, O red, Cu violet.

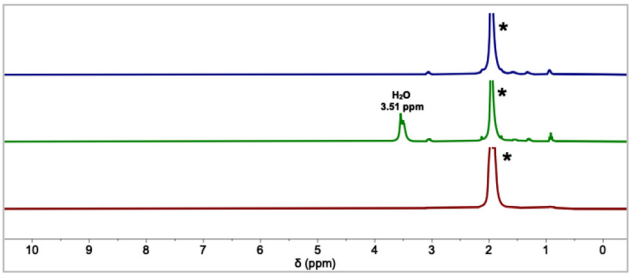

Fig. 8 ^{1}H-NMR spectra of the pre-electrolysis solution (brown trace), post electrolysis solution with CH_3COOH (green trace) and with CD_3COOD (blue trace). '*' denotes the signal for the solvent acetonitrile.

H_2O, ^{1}H-NMR spectra of the electrolyte solution before and after electrolysis were recorded. In the ^{1}H-NMR spectrum of the electrocatalytic solution (solvent CD_3CN/D_2O 100 : 1) before electrolysis we did not observe any peak for water but in the case of the post-electrolysis solution a new peak at 3.51 ppm was observed (Fig. 8). To confirm that the peak at 3.51 ppm is indeed originating from H_2O, the ^{1}H-NMR spectrum was recorded for an identical electrolyte solution with water externally added to it. A rise of the peak at 3.51 ppm was observed in the spectrum, which gives conclusive proof that the peak corresponds to the protons of water (Fig. S17†). Furthermore, the entire electrolysis process was repeated with the deuterated reagent acetic acid-d$_4$ (CD_3COOD) and this was tracked by ^{1}H-NMR. In this ^{1}H-NMR spectrum, no peak for water was found (Fig. 8). Therefore, it can be inferred that the protons of the water molecule come from acetic acid.

Conclusion

In summary, a new copper-based complex (**1**) was synthesized that is capable of reducing NO_2^- electrochemically to NO at −1.29 V *vs.* Fc^+/Fc with FE_{NO} of 81%. We have managed to isolate and deduce molecular structures for the majority of the intermediate species involved in the mechanistic cycle. In particular, concrete structural proof for the linkage isomerism of NO_2^- upon reduction of Cu^{II} to Cu^{I} was acquired by isolating and crystallizing the intermediate $TerpyCu^{I}$ species. Additionally, we have successfully determined the post-electrolysis state of the catalyst and electrode *via* SXRD and SEM/EDX analysis, respectively. Through, isotope-labelling experiments using ^{15}N-labelled $Na^{15}NO_2$ (the nitrite source) we have established that the N in NO and N_2O indeed comes from the nitrite source. Likewise, using deuterated acetic acid, CD_3COOD (the D^+ source), it was demonstrated that acetic acid is the proton source during the entire conversion process and that the H atoms of the side-product water originate from acetic acid.

These results give us important insight about the mechanistic route involving rearrangement from O-bound to N-bound nitrite. Our report showcases a wide canvas of NO_2^- conversion with great structural detail that may aid future designs of new molecular catalysts for conversion of NO_x or other small molecules. It is believed that the intermediates could also be very handy for the activation of some other species.

Experimental section

General techniques

All reactions were carried out under air unless otherwise stated. To conduct synthesis under an inert atmosphere, the standard Schlenk technique or an MBraun UNIlab^{ECO} glovebox was used with dry or degassed solvents. Reagents, *e.g.* the **Terpy** ligand, and metal salts were purchased from commercial vendors and used directly without further purification. Solvents were dried using an MBraun SPS solvent purification system or by following standard methods. ^{1}H-NMR spectroscopy was conducted at room temperature with Bruker

AVIII-400 and AVIII-300 spectrometers and chemical shifts are reported in ppm. Mass spectra of samples were recorded in acetonitrile solvent using a Bruker ESQ 3000 spectrometer. IR studies were done with a Shimadzu IRTracer-100 equipped with a Pike Miracle ATR unit and spectra are reported in wavenumbers (cm^{-1}). UV-Vis measurements were done with a Shimadzu UV-1900i spectrometer at room temperature and are reported in nm. CHN elemental analysis was done with an Elementar Vario MICRO cube. Suitable single crystals were analyzed using a RigakuXTAlab Synergy diffractometer (Cu Kα, λ = 1.54184 Å) to which was attached a HyPix-6000HE detector. The recorded data were processed and analyzed with CrysAlisPro and Platon software.[65] The structures were solved using SHELXT[66] and refined against F^2 (SHELXL).[67] OLEX^2 software was used to generate graphics and pictures.[68] Detailed crystallographic data are provided in the ESI.†

Synthetic procedures

[TerpyCu(CH_3CN)](ClO_4)$_2$, (1). 0.1 mmol (23.3 mg) Terpy (Terpy = 2,2′:6′,2″-terpyridine) was dissolved in 4 mL of acetonitrile. To this solution 1 mL of an acetonitrile solution of 0.1 mmol (37.0 mg) $Cu(ClO_4)_2{\cdot}6H_2O$ was added. Upon addition of the Cu^{II} salt the mixture instantly turned dark blue from pale yellow. The mixture was stirred for 1 h at room temperature. After 1 h, the solvent was evaporated, and the solid residues were thoroughly washed with diethyl ether and dried under reduced pressure. The solid was then redissolved in 3 mL of a solvent mixture of acetonitrile/methanol (4 : 1) and filtered. The filtrate was then evaporated to obtain blue-coloured complex **1** with yield of 84%. Single crystals for SXRD analysis were obtained from layering an acetonitrile solution of **1** on top of a dichloromethane (CH_2Cl_2) layer at −6 °C. ESI-MS: calcd for $[TerpyCu(ClO_4)]^+$ *m*/*z* 394.97, found 395.0; calcd for $[TerpyCu]^+$ *m*/*z* 296.02, found 296.0. FT-IR (KBr): 3033 (m) (ν_s ^{Ar}C–H); 1596 (m), 1576 (w) (ν_s C=N); 1499 (w), 1472 (s), 1449 (s) (ν_s C=C); 1406 (w), 1383 (m), 1330 (m), 1303 (m), 1113 (s) (ν_s ClO_4^-); 1019 (m); 970 (w); 940 (w); 908 (w); 828 (w); 777 (s); 729 (m) cm^{-1}. Magnetic moment (^{1}H-NMR using Evans' method): 1.69 BM. UV-Vis: λ_{max} 626 nm (ε 113.6 L mol^{-1} cm^{-1}). Elemental analysis (%): calcd C 38.0, H 2.6, N 10.4; found C 37.7, H 3.0, N 9.7.

[(Terpy)$_2$Cu](ClO_4)$_2$, (2). The synthesis was performed with little alteration to the previously reported method.[53] 0.1 mmol (23.3 mg) Terpy was dissolved in 5 mL of acetonitrile. To this solution a 1 mL solution of 0.04 mmol (14.8 mg) $Cu(ClO_4)_2{\cdot}6H_2O$ was added. After adding the metal salt, the solution turned green. The reaction mixture was stirred for 1 h at room temperature. Green solid was obtained by evaporating the solvent under reduced pressure. The solid compound was then washed with diethyl ether. After that, it was redissolved in acetonitrile and filtered. Crude green-coloured compound **2** was obtained in 71% yield after evaporating the filtrate under reduced pressure. Single crystals for SXRD analysis were obtained from layering a solution of **2** on top of a dichloromethane layer at room temperature. ESI-MS: calcd for $[(Terpy)_2Cu]^{2+}$ *m*/*z* 264.56, found 264.6. FT-IR (KBr): 3088 (s) (ν_s ^{Ar}C–H); 1601 (m), 1576 (s) (ν_s C=N); 1501 (w), 1476 (s), 1452 (ν_s C=C); 1404 (w), 1384(w), 1318(m), 1247 (m) (ν_s C–N); 1194 (w), 1167 (w), 1090 (s) (ν_s ClO_4^-); 1012 (w); 973 (w); 920 (w); 899 (w); 829 (w); 771 (s); 733 (w) cm^{-1}. UV-Vis: λ_{max} 690 nm (ε 65.0 L mol^{-1} cm^{-1}). Elemental analysis (%): calcd C 49.0, H 3.1, N 11.4; found C 49.0, H 3.1, N 11.4.

[TerpyCu(ONO)]ClO_4, (1-ONO). First, **1** was prepared and isolated according to the method described above. To the acetonitrile solution of **1** (0.1 mmol), 0.1 mmol (6.9 mg) $NaNO_2$ in a CH_3OH/H_2O mixture (H_2O in trace amount) was added. Upon addition of $NaNO_2$, the blue-coloured solution of **1** immediately turned green. The mixture was stirred for 2 h. After 2 h, a dark green solid crude product was obtained by evaporation of the solvent. The solid residue was thoroughly washed with diethyl ether and dried under reduced pressure. The solid was then redissolved in 5 mL of acetonitrile and filtered. The filtrate was then evaporated to obtain the green-coloured **1-ONO** compound in 82% yield. Single crystals for SXRD analysis were obtained from layering an acetonitrile solution of **1-ONO** on top of a dichloromethane (CH_2Cl_2) layer at −6 °C.

1-ONO can also be synthesised by direct addition of $NaNO_2$ in the reaction solution of **1** without isolating it. However, the yield (71%) of the product in this method was lower compared to that of the former. ESI-MS: calcd for $[TerpyCu(ONO)]^+$ *m*/*z* 342.02, found 342.1. FT-IR (KBr): 3042 (m) (ν_s ^{Ar}C–H); 1597 (s), 1575 (m) (ν_s C=N); 1498 (m), 1473 (s), 1449 (s) (ν_s C=C); 1405 (w), 1384 (w), 1366 (w) (ν_{asym}, NO_2); 1329 (m), 1303 (m), 1268 (s) (ν_{sym}, NO_2); 1111 (s) (ν_s ClO_4^-); 1034 (w); 1019 (m); 972 (w); 940 (w); 907 (w); 827 (w); 779 (s); 731 (m) cm^{-1}. UV-Vis: λ_{max} 372 nm (ε 364 L mol^{-1} cm^{-1}) and λ_{max} 640 nm (ε 54 L mol^{-1} cm^{-1}). Elemental analysis (%): calcd C 40.7, H 2.5, N 12.7; found C 40.6, H 2.8, N 13.1.

[TerpyCu(O^{15}NO)]ClO_4, (1-O^{15}NO). The synthesis was performed following the same method as that for **1-ONO** except 0.1 mmol (7.0 mg) $Na^{15}NO_2$ was used in this case. Yield 71%. ESI-MS: calcd for $[TerpyCu(O^{15}NO)]^+$ *m*/*z* 343.02, found 343.02. FT-IR (KBr): 3033 (m) (ν_s ^{Ar}C–H); 1598 (s), 1574 (m) (ν_s C=N); 1500 (m), 1472 (s), 1450 (s) (ν_s C=C); 1406 (w), 1384 (w), 1352 (ν_{asym}, $^{15}NO_2$); 1332 (m), 1302 (m), 1251 (ν_{sym}, $^{15}NO_2$); 1118 (s) (ν_s ClO_4^-); 1019 (w); 972 (w); 940 (w); 908 (w); 828 (w); 776 (w); 730 (m) cm^{-1}.

[TerpyCu(NO_2)]$_2$, (4). 0.1 mmol (31.4 mg) of $[Cu(CH_3CN)_4]BF_4$ was dissolved in 1 mL of dry acetonitrile and this solution was then added to a 1 mL dry acetonitrile solution containing 0.1 mmol (23.3 mg) Terpy. Upon addition of the metal salt, the colourless ligand solution instantly turned dark brown. The reaction mixture was stirred for 10 min under an inert atmosphere inside a glovebox. After 10 min, 0.1 mmol $NaNO_2$ (6.9 mg) in a minimum volume mixture of degassed CH_3OH/H_2O was added to the reaction mixture and this was stirred for another 5 min. A dark brown solid was obtained upon evaporating the solvent under reduced pressure. The solid was quickly washed with dry diethyl ether and redissolved in a minimum volume of dry acetonitrile. The acetonitrile solution was then filtered, and the filtrate was evaporated under reduced pressure to produce **4** as a dark brown solid in 69%

yield. Here it is worth mentioning that if this compound is stored for any length of time, then the Cu^{I} starts to disproportionate to Cu^{II} and Cu^{0}, which is a common phenomenon for Cu^{I} complexes. Single crystals were obtained from a CH_3CN solution by vapour diffusion of diethyl ether at −35 °C. ESI-MS: calcd for $[(TerpyCu(CH_3CN))_2]^{2+}$ m/z 337.05, found m/z 337.05; calcd for $[(TerpyCu(NO_2))_2 + 2CH_3CN + CH_3OH + H_2O + 2H^+]^{2+}$ m/z 409.07, found m/z 409.07. FT-IR: 3063 (m) (ν_s ^{Ar}C–H); 1650 (w), 1599 (m), 1580 (w), 1561 (m) (ν_s C=N); 1471 (s), 1452 (s) (ν_s C=C); 1421 (w), 1383 (w), 1325 (w) (ν_{asym}, NO_2; 1295 for $^{15}NO_2$); 1270 (ν_{sym}, NO_2; 1243 for $^{15}NO_2$); 1059 (s) (ν_s BF_4^-); 881 (w); 832 (w); 780 (s); 735 (w); 670 (w); 651 (w); 630 (w) cm^{-1}. UV-Vis: λ_{max} 370 nm (ε 900 L mol^{-1} cm^{-1}).[69] No paramagnetically shifted signal was observed in the long-range paramagnetic NMR. The ^{1}H-NMR spectrum was recorded as described in Evans' method;[70,71] no shift in the acetonitrile peak was observed.

Crystallographic data

See the ESI, pages S18–S24.†

Experimental details of the electrochemical experiments

Electrochemical experiments were performed with a standard three-electrode setup (glassy carbon working electrode, Pt wire counter electrode and Ag wire as pseudo-reference electrode) using a PalmSens4 potentiostat. The working electrode was prepared by polishing the glassy carbon with 1.0 and 0.3 μm alumina solution and then subsequently subjecting it to sonication in the applied solvent for 30 min before using. Tetrabutylammonium hexafluorophosphate ($^nBu_4NPF_6$) (0.1 M in the case of CV and 0.2 M in the case of CA) was used as a supporting electrolyte. All the electrochemical measurements were done under an inert atmosphere inside a glovebox. Since Ag wire is a pseudo-reference electrode, the potentials of all the redox events were referenced against a ferrocene/ferrocenium (Fc^+/Fc) redox couple.

All CV experiments were performed in MeCN containing 1 mM **1**, 150 mM CH_3COOH and 0.1 M $^nBu_4NPF_6$. A $NaNO_2$ stock solution in water was prepared from which specific aliquots were extracted and added during different CV measurements. Cyclic voltammograms were recorded in the presence of 5 mM, 10 mM and 20 mM NO_2^-, with the total electrolyte volume maintained at 2 mL for all experiments. All scans were recorded at a scan rate of 100 mV s^{-1}.

Bulk electrolysis (chronoamperometry) was performed with the same setup as mentioned above. The electrolysis was performed in a solvent mixture of MeCN/H_2O (100 : 1) containing 2 mM **1**, 150 mM CH_3COOH, 40 mM $NaNO_2$ and 0.2 M $^nBu_4NPF_6$. Separate bulk electrolysis experiments were conducted with durations of 1 h, 3 h, 5 h and 7 h. For all the experiments the potential was fixed at −1.29 V.

Furthermore, to determine the catalytically active species, a rinse test was performed. First, a chronoamperometric experiment was carried out by holding the reductive potential at $Cu^{I} \rightarrow Cu^{0}$ resulting in the deposition of metallic copper on the electrode surface. Subsequently, the electrochemical cell was replenished with a fresh solution containing 5 mM $NaNO_2$ and 150 mM CH_3COOH, without altering the working electrode. Then, linear sweep voltammetry (LSV) was performed to monitor the current response of the deposited material. For comparison, an LSV scan was also recorded for a solution containing 2 mM compound **1**, 150 mM CH_3COOH and 5 mM sodium nitrite.

Spectroscopic detection of NO using CoTPP

A small, uncapped vial containing 1 mL of 40 μM CoTPP solution in THF, was attached to the inner wall of the electrochemical cell in such a way that the CoTPP solution does not come into contact with the electrolyte solution. The electrochemical cell was sealed under an inert atmosphere, and bulk electrolysis was performed under these conditions and setup. The vial of CoTPP was kept open so that the $NO_{(g)}$, which accumulated in the headspace, can diffuse into the CoTPP solution and coordinate with the Co^{II} centre. The whole operation was carried out under an inert atmosphere. After that, the CoTPP solution was removed and diluted to 8 μM and UV-Vis spectra were recorded showing a shift of the 527 nm band of CoTPP to 535 nm.

Experimental details of GC-MS analysis for NO and N_2O detection

GC-MS analyses were done using a Shimadzu GC-MS-QP2010 Plus instrument with a flame ionized detector (FID) and a HP-Plot-Q column of 30 m length, inner diameter of 0.53 mm and a thickness of 40 μm.

Starting temperature: 35 °C, hold time: 2 min; ramp: 25 °C min^{-1} to 240 °C, split ratio: 20.0; pressure: 30 kPa. Flow rate: 66.7 mL min^{-1}; carrier gas: helium (He). Retention time: R_t (NO) = 3.78 min, R_t (N_2O) = 5.37 min.

Data availability

All data supporting these findings can be found in the article and its ESI† or are available from the authors upon reasonable request.

Conflicts of interest

The authors declare no conflict of interest.

Acknowledgements

This work was supported by the Deutsche Forschungsgemeinschaft (DFG; German Research Foundation) for financial support under Germany's Excellence Strategy – (EXC-2033 390677874 – "RESOLV" and AP242/9-1). This work was further supported by the Fraunhofer Internal Programs under Grant No. Attract 097- 602175. Likewise, this work was also supported by Grants-in-Aid (Grant No. CRG/2021/003371, and EEQ/2021/000109) from SERB, and DAAD (ID: 57552334).

References

1 L. Y. Stein and M. G. Klotz, *Curr. Biol.*, 2016, **26**, R94–R98.
2 M. M. M. Kuypers, H. K. Marchant and B. Kartal, *Nat. Rev. Microbiol.*, 2018, **16**, 263–276.
3 W. Steffen, K. Richardson, J. Rockström, S. E. Cornell, I. Fetzer, E. M. Bennett, R. Biggs, S. R. Carpenter, W. de Vries, C. A. de Wit, C. Folke, D. Gerten, J. Heinke, G. M. Mace, L. M. Persson, V. Ramanathan, B. Reyers and S. Sörlin, *Science*, 2015, **347**, 1259855.
4 K. Richardson, W. Steffen, W. Lucht, J. Bendtsen, S. E. Cornell, J. F. Donges, M. Drüke, I. Fetzer, G. Bala, W. von Bloh, G. Feulner, S. Fiedler, D. Gerten, T. Gleeson, M. Hofmann, W. Huiskamp, M. Kummu, C. Mohan, D. Nogués-Bravo, S. Petri, M. Porkka, S. Rahmstorf, S. Schaphoff, K. Thonicke, A. Tobian, V. Virkki, L. Wang-Erlandsson, L. Weber and J. Rockström, *Sci. Adv.*, 2023, **9**, eadh2458.
5 D. Gerten, V. Heck, J. Jägermeyr, B. L. Bodirsky, I. Fetzer, M. Jalava, M. Kummu, W. Lucht, J. Rockström, S. Schaphoff and H. J. Schellnhuber, *Nat. Sustain.*, 2020, **3**, 200–208.
6 L. B. Maia and J. J. G. Moura, *Chem. Rev.*, 2014, **114**, 5273–5357.
7 L. Lamattina, C. García-Mata, M. Graziano and G. Pagnussat, *Annu. Rev. Plant Biol.*, 2003, **54**, 109–136.
8 V. Calabrese, C. Mancuso, M. Calvani, E. Rizzarelli, D. A. Butterfield and A. M. G. Stella, *Nat. Rev. Neurosci.*, 2007, **8**, 766–775.
9 S. A. Omar and A. J. Webb, *J. Mol. Cell. Cardiol.*, 2014, **73**, 57–69.
10 J. Heinecke and P. C. Ford, *Coord. Chem. Rev.*, 2010, **254**, 235–247.
11 G. R. Navale, S. Singh and K. Ghosh, *Coord. Chem. Rev.*, 2023, **481**, 215052.
12 M. T. Gladwin, A. N. Schechter, D. B. Kim-Shapiro, R. P. Patel, N. Hogg, S. Shiva, R. O. Cannon, M. Kelm, D. A. Wink, M. G. Espey, E. H. Oldfield, R. M. Pluta, B. A. Freeman, J. R. Lancaster, M. Feelisch and J. O. Lundberg, *Nat. Chem. Biol.*, 2005, **1**, 308–314.
13 J. O. Lundberg, E. Weitzberg and M. T. Gladwin, *Nat. Rev. Drug Discovery*, 2008, **7**, 156–167.
14 K. Cosby, K. S. Partovi, J. H. Crawford, R. P. Patel, C. D. Reiter, S. Martyr, B. K. Yang, M. A. Waclawiw, G. Zalos, X. Xu, K. T. Huang, H. Shields, D. B. Kim-Shapiro, A. N. Schechter, R. O. Cannon and M. T. Gladwin, *Nat. Med.*, 2003, **9**, 1498–1505.
15 R. G. Knowles and S. Moncada, *Biochem. J.*, 1994, **298**(Pt 2), 249–258.
16 T. B. McCall, N. K. Boughton-Smith, R. M. Palmer, B. J. Whittle and S. Moncada, *Biochem. J.*, 1989, **261**, 293–296.
17 S. Basu, N. A. Azarova, M. D. Font, S. B. King, N. Hogg, M. T. Gladwin, S. Shiva and D. B. Kim-Shapiro, *J. Biol. Chem.*, 2008, **283**, 32590–32597.
18 F. Cava, O. Zafra and J. Berenguer, *Mol. Microbiol.*, 2008, **70**, 507–518.
19 S. Shahid, M. Ali, D. Legaspi-Humiston, J. Wilcoxen and A. A. Pacheco, *Biochemistry*, 2021, **60**, 2098–2115.
20 B. L. J. Godber, J. J. Doel, G. P. Sapkota, D. R. Blake, C. R. Stevens, R. Eisenthal and R. Harrison, *J. Biol. Chem.*, 2000, **275**, 7757–7763.
21 L. B. Maia and J. J. G. Moura, *J. Biol. Inorg. Chem.*, 2011, **16**, 443–460.
22 L. B. Maia and J. J. G. Moura, *Redox Biol.*, 2018, **19**, 274–289.
23 B. A. Averill, *Chem. Rev.*, 1996, **96**, 2951–2964.
24 E. I. Solomon, D. E. Heppner, E. M. Johnston, J. W. Ginsbach, J. Cirera, M. Qayyum, M. T. Kieber-Emmons, C. H. Kjaergaard, R. G. Hadt and L. Tian, *Chem. Rev.*, 2014, **114**, 3659–3853.
25 S. Horrell, D. Kekilli, R. W. Strange and M. A. Hough, *Metallomics*, 2017, **9**, 1470–1482.
26 J. W. Godden, S. Turley, D. C. Teller, E. T. Adman, M. Y. Liu, W. J. Payne and J. LeGall, *Science*, 1991, **253**, 438–442.
27 F. E. Dodd, S. S. Hasnain, Z. H. Abraham, R. R. Eady and B. E. Smith, *Acta Crystallogr., Sect. D:Biol. Crystallogr.*, 1997, **53**, 406–418.
28 M. E. P. Murphy, S. Turley and E. T. Adman, *J. Biol. Chem.*, 1997, **272**, 28455–28460.
29 M. J. Boulanger and M. E. P. Murphy, *Protein Sci.*, 2003, **12**, 248–256.
30 S. V. Antonyuk, R. W. Strange, G. Sawers, R. R. Eady and S. S. Hasnain, *Proc. Natl. Acad. Sci. U. S. A.*, 2005, **102**, 12041–12046.
31 S. Ghosh, A. Dey, Y. Sun, C. P. Scholes and E. I. Solomon, *J. Am. Chem. Soc.*, 2009, **131**, 277–288.
32 I. M. Wasser, S. de Vries, P. Moënne-Loccoz, I. Schröder and K. D. Karlin, *Chem. Rev.*, 2002, **102**, 1201–1234.
33 S. M. Carrier, C. E. Ruggiero, W. B. Tolman and G. B. Jameson, *J. Am. Chem. Soc.*, 1992, **114**, 4407–4408.
34 E. I. Tocheva, F. I. Rosell, A. G. Mauk and M. E. P. Murphy, *Science*, 2004, **304**, 867–870.
35 K. Fujisawa, A. Tateda, Y. Miyashita, K. Okamoto, F. Paulat, V. K. K. Praneeth, A. Merkle and N. Lehnert, *J. Am. Chem. Soc.*, 2008, **130**, 1205–1213.
36 S. Hong, J. J. Yan, D. G. Karmalkar, K. D. Sutherlin, J. Kim, Y.-M. Lee, Y. Goo, P. K. Mascharak, B. Hedman, K. O. Hodgson, K. D. Karlin, E. I. Solomon and W. Nam, *Chem. Sci.*, 2018, **9**, 6952–6960.
37 J. Biswas, K. Kulbir, P. Bhardwaj, S. Ghosh, S. C. Sahoo, U.-P. Apfel and P. Kumar, *Chem. – Eur. J.*, 2024, e202402295.
38 N. Komeda, H. Nagao, G. Adachi, M. Suzuki, A. Uehara and K. Tanaka, *Chem. Lett.*, 1993, **22**, 1521–1524.
39 N. Komeda, H. Nagao, Y. Kushi, G. Adachi, M. Suzuki, A. Uehara and K. Tanaka, *Bull. Chem. Soc. Jpn.*, 1995, **68**, 581–589.

40 H. Ren, J. Wu, C. Xi, N. Lehnert, T. Major, R. H. Bartlett and M. E. Meyerhoff, *ACS Appl. Mater. Interfaces*, 2014, **6**, 3779–3783.
41 Y. Qin, J. Zajda, E. J. Brisbois, H. Ren, J. M. Toomasian, T. C. Major, A. Rojas-Pena, B. Carr, T. Johnson, J. W. Haft, R. H. Bartlett, A. P. Hunt, N. Lehnert and M. E. Meyerhoff, *Mol. Pharmaceutics*, 2017, **14**, 3762–3771.
42 K. K. Konopińska, N. J. Schmidt, A. P. Hunt, N. Lehnert, J. Wu, C. Xi and M. E. Meyerhoff, *ACS Appl. Mater. Interfaces*, 2018, **10**, 25047–25055.
43 G. Cioncoloni, I. Roger, P. S. Wheatley, C. Wilson, R. E. Morris, S. Sproules and M. D. Symes, *ACS Catal.*, 2018, **8**, 5070–5084.
44 S. E. Braley, H.-Y. Kwon, S. Xu, E. Z. Dalton, E. Jakubikova and J. M. Smith, *Inorg. Chem.*, 2022, **61**, 12998–13006.
45 J. R. Stroka, B. Kandemir, E. M. Matson and K. L. Bren, *ACS Catal.*, 2020, **10**, 13968–13972.
46 P. H. van Langevelde, S. Engbers, F. Buda and D. G. H. Hetterscheid, *ACS Catal.*, 2023, **13**, 10094–10103.
47 Kulbir, S. Das, T. Devi, M. Goswami, M. Yenuganti, P. Bhardwaj, S. Ghosh, S. C. Sahoo and P. Kumar, *Chem. Sci.*, 2021, **12**, 10605–10612.
48 Kulbir, S. Das, T. Devi, S. Ghosh, S. C. Sahoo and P. Kumar, *Chem. Sci.*, 2023, **14**, 2935–2942.
49 Kulbir, A. Keerthi C. S, S. Beegam, S. Das, P. Bhardwaj, M. Ansari, K. Singh and P. Kumar, *Inorg. Chem.*, 2023, **62**, 7385–7392.
50 S. Das, Kulbir, S. Ray, T. Devi, S. Ghosh, S. S. Harmalkar, S. N. Dhuri, P. Mondal and P. Kumar, *Chem. Sci.*, 2022, **13**, 1706–1714.
51 K. Ghosh, A. A. Eroy-Reveles, B. Avila, T. R. Holman, M. M. Olmstead and P. K. Mascharak, *Inorg. Chem.*, 2004, **43**, 2988–2997.
52 A. J. Amoroso, M. W. Burrows, S. J. Coles, R. Haigh, R. D. Farley, M. B. Hursthouse, M. Jones, K. M. A. Malik and D. M. Murphy, *Dalton Trans.*, 2008, 506–513.
53 J. Karges, K. Xiong, O. Blacque, H. Chao and G. Gasser, *Inorg. Chim. Acta*, 2021, **516**, 120137.
54 A. Meyer, G. Schnakenburg, R. Glaum and O. Schiemann, *Inorg. Chem.*, 2015, **54**, 8456–8464.
55 H. A. Benesi and J. H. Hildebrand, *J. Am. Chem. Soc.*, 1949, **71**, 2703–2707.
56 A. K. Purohit, S. K. Padhan, J. R. Mohanty and P. K. Kar, *Photochem. Photobiol. Sci.*, 2018, **17**, 815–821.
57 A. Dey, T. Albert, R. Y. Kong, S. N. MacMillan, P. Moënne-Loccoz, K. M. Lancaster and D. P. Goldberg, *Inorg. Chem.*, 2022, **61**, 14909–14917.
58 S. Metz, *Inorg. Chem.*, 2017, **56**, 3820–3833.
59 C. E. Ruggiero, S. M. Carrier and W. B. Tolman, *Angew. Chem., Int. Ed. Engl.*, 1994, **33**, 895–897.
60 C. J. Hoerger, H. S. L. Pierre, L. Maron, A. Scheurer, F. W. Heinemann and K. Meyer, *Chem. Commun.*, 2016, **52**, 10854–10857.
61 X. Zhang, Y. Wang, Y. Wang, Y. Guo, X. Xie, Y. Yu and B. Zhang, *Chem. Commun.*, 2022, **58**, 2777–2787.
62 S. Xu, H.-Y. Kwon, D. C. Ashley, C.-H. Chen, E. Jakubikova and J. M. Smith, *Inorg. Chem.*, 2019, **58**, 9443–9451.
63 Y. Arikawa, Y. Otsubo, H. Fujino, S. Horiuchi, E. Sakuda and K. Umakoshi, *J. Am. Chem. Soc.*, 2018, **140**, 842–847.
64 R. C. Maji, S. K. Barman, S. Roy, S. K. Chatterjee, F. L. Bowles, M. M. Olmstead and A. K. Patra, *Inorg. Chem.*, 2013, **52**, 11084–11095.
65 A. L. Spek, *J. Appl. Crystallogr.*, 2003, **36**, 7–13.
66 G. M. Sheldrick, *Acta Crystallogr., Sect. A:Found. Adv.*, 2015, **71**, 3–8.
67 G. M. Sheldrick, *Acta Crystallogr., Sect. C:Struct. Chem.*, 2015, **71**, 3–8.
68 O. V. Dolomanov, L. J. Bourhis, R. J. Gildea, J. a. K. Howard and H. Puschmann, *J. Appl. Crystallogr.*, 2009, **42**, 339–341.
69 J. Jökel, F. Nyßen, D. Siegmund and U.-P. Apfel, *Dalton Trans.*, 2021, **50**, 14602–14610.
70 D. F. Evans, *J. Chem. Soc.*, 1959, 2003–2005.
71 J. Loliger and R. Scheffold, *J. Chem. Educ.*, 1972, **49**, 646.